GW space-time method: Energy band gap of solid hydrogen

Sam Azadi[*]
Department of Physics, Clarendon Laboratory, University of Oxford, Parks Road, Oxford OX1 3PU, United Kingdom and Department of Physics, King's College London, Strand, London WC2R 2LS, United Kingdom

Arkadiy Davydov[†]
Department of Physics, King's College London, Strand, London WC2R 2LS, United Kingdom Physik-Institut, University of Zurich, 8057 Zurich, Switzerland; and Scientific Computing Research Technology Platform, University of Warwick, Zeeman Building, CV4 7AL, Coventry, United Kingdom

Evgeny Kozik
Department of Physics, King's College London, Strand, London WC2R 2LS, United Kingdom

(Received 24 October 2020; revised 2 March 2022; accepted 6 April 2022; published 19 April 2022)

We implement the *GW* space-time method at finite temperatures, in which the Green's function G and the screened Coulomb interaction W are represented in the real space on a suitable mesh and in imaginary time in terms of Chebyshev polynomials, paying particular attention to controlling systematic errors of the representation. Having validated the technique by the canonical application to silicon and germanium, we apply it to the calculation of band gaps in hexagonal solid hydrogen with the bare Green's function obtained from density functional approximation and the interaction screened within the random phase approximation. The results, obtained from the asymptotic decay of the full Green's function without resorting to analytic continuation, suggest that the solid hydrogen above 150 GPa cannot adopt an orientationally ordered hexagonal-closed-pack structure due to its metallic behavior. The demonstrated ability of the method to store the full G and W functions in memory with sufficient accuracy is crucial for its subsequent extensions to include higher orders of the diagrammatic series by means of diagrammatic Monte Carlo algorithms.

DOI: 10.1103/PhysRevB.105.155136

I. INTRODUCTION

The metallization of solid hydrogen at low temperatures under extremely high pressures is an open challenging problem in condensed matter physics and materials science. It has been a subject of intensive studies since 1935 [1]—by experiment, theory, and, more recently, computational techniques—stimulated, in particular, by the possibility that metallic hydrogen is a room-temperature superconductor, driven by conventional phonon-mediated mechanisms [2], harbors a new phase of matter in the low-temperature liquid state [3,4], and can be found inside giant planets [5–7]. Nonetheless, determining the metallization mechanism and metallization pressure of solid hydrogen is still a controversial subject.

Up to pressures of 430 GPa, around or beyond which the metallic state is expected to emerge, the detection of vibron excitations evidences that solid hydrogen is in a molecular form [8]. Thus, metallization is likely to emerge with compression either by a continuous closure of the energy band gap in a molecular crystal, or by a structural phase transition from the molecular insulator to an atomic or molecular metal. However, because determining the band gap experimentally under extreme conditions is very difficult, the available data are limited [8]. From the theoretical perspective, which metallization scenario is realized largely depends on the specific crystal structure assumed in the calculation. At the same time, despite an extensive amount of work by experiment [8–18] and theory [19–36], there is no definitive conclusion on the crystal structure of solid hydrogen in the range of pressures where any of the metallization scenarios might take place. It was recently observed in x-ray diffraction measurements [37] that, at least up to 250 GPa, solid hydrogen remains in the hexagonal-closed-pack (hcp) crystal form, albeit possibly with an increasingly under compression anisotropy. It is therefore important to evaluate the pressure at which solid hydrogen becomes metallic by band-gap closure, provided it remains an hcp crystal. This is the problem addressed by our work.

With the lack of direct experimental access, advanced computational techniques play a crucial role in elucidating the behavior of the band gap under compression. The diffusion quantum Monte Carlo (DMC) and variational quantum Monte Carlo (VMC) methods can be efficiently used to obtain the excitation energies above the ground state in a finite-size (FS) system, but the extrapolation to the thermodynamic limit is typically challenging [38,39]. DMC calculations of excitation properties suffer from the simulation cell finite-size ($1/L$)

[*]sam.azadi@physics.ox.ac.uk
[†]adavydov@physik.uzh.ch

errors and the $1/N$ effect: the variation in the total ground-state energy due to the presence of a one- or two-particle excitations is inversely proportional to the number of electrons N in the simulation cell. The large number of atoms per primitive cell in almost all of the predicted for solid hydrogen structures makes controlling the FS errors especially difficult.

An efficient approach to describing excitation properties directly in the thermodynamic limit is provided by the many-body perturbation theory in terms of Feynman diagrams. In this framework, the lowest order in terms of the Green's function G and screened Coulomb interaction W GW approximation has been most widely used [40–42]. The accuracy of the GW approach, assessed by comparison of the results with the experiment, can vary with the kind of approximation applied to G and W themselves. The natural self-consistent approach [43,44]—in which G is determined by the self-energy in terms of G, $\Sigma = -GW$, with W screened by the polarization given by GG—is known to overestimate the valence bandwidth of the Ge and Si crystals [45,46]. This discrepancy can be efficiently addressed [47,48], even in more challenging cases, such as MnO and NiO, by the quasiparticle self-consistent GW approach [49,50] (QSGW), in which G is derived from an effective single-particle Hamiltonian constructed self-consistently using Σ as the exchange-correlation contribution, which makes the result independent of the initial input. Although one advantage of self-consistent GW is to eliminate the dependence of final results on the one-particle starting point, a fully self-consistent GW approach without vertex corrections has certain theoretical problems and corresponding calculations overestimate band gaps in semiconductors and insulators, and bandwidths in metals [51,52]. However, in many cases the so-called "*one-shot*" G_0W_0 method is deemed sufficiently accurate [53], especially for the calculations of the band gap of solid hydrogen [54]. Applying the first-order vertex correction to the polarizibility and to the self-energy indicates that vertex corrections and self-consistence diagrams cancel out to a high degree that provides a justification for the one-shot G_0W_0 approach [55]. Here, for Si and Ge, G and W are built with the exchange-correlation potential in the local-density approximation (LDA) of the density functional theory (DFT), and the self-energy determines the correction to the LDA quasiparticle energies, as explained in the next section. In the case of solid hydrogen, however, the main results were obtained with the Becke-Lee-Yang-Parr (BLYP) approximation for the exchange-correlation potential of DFT part, as it provides a slightly better starting point for the many-body expansion.

Applying the finite-temperature Green's function formalism to real systems with the "chemical accuracy" is a formidable task because the eigenvalue spectrum of realistic Hamiltonians is wide. In this work, we develop an efficient implementation of the GW space-time (GWST) method [56–59] in which the functions G and W are constructed in real space and imaginary time at finite temperature. The quasiparticle excitation energies are typically obtained with the help of analytic continuation of the self-energy to the real frequency domain, which is a difficult problem in itself and a source of additional systematic errors. The finite-temperature formalism allows us to extract band gaps in a controlled way from the asymptotic behavior of the full many-body Green's function at large imaginary times. More generally, we demonstrate control of all systematic errors apart from that of the GW approximation, concluding that the employed Chebyshev polynomial representation [60,61] suits this purpose quite well. An important feature of our approach is that the G and W functions are represented and stored in memory in full, which makes it amenable to immediate extension to higher orders of the diagrammatic expansion by means of stochastic sampling of the series using the diagrammatic Monte Carlo (DiagMC) technique [62–68].

We apply our approach to evaluate the direct and indirect band gaps of the hcp solid hydrogen under compression. To this end, we perform one-shot GW calculations, the accuracy of which is expected to be comparable to that of more advanced GW schemes due to the chemically primitive composition of the system, involving only s electrons. We first validate this approach by reproducing benchmarks for the Si and Ge crystals, which are well understood both experimentally and numerically. We then study the energy band-gap reduction in hcp solid hydrogen as a function of pressure. With a speculation on the role of lattice dynamics and vibrons in decreasing the band gap, we conclude that the solid hydrogen above 150 GPa cannot adopt the orientationally ordered hcp crystal structure. Obtained with new analytic continuation free approach, this result confirms the earlier studies [69].

The paper is organized as follows. Section II consist of two parts. Section II A describes, at the conceptual level, the GWST method and our approach to the energy band-gap calculation. In Sec. II B, we discuss more technical details, including those of the underlying DFT calculations and numerical representation of the G and W functions in imaginary time. In Sec. III we demonstrate our new work flow for the band-gap extraction from the Green's function asymptotic behavior (Sec. III A) and extrapolation to the infinity of the discretization parameters (Sec. III B) using a test set of materials. We present and discuss our results for solid hydrogen in the context of the available experimental data in Sec IV. Section V concludes the paper.

II. *GW* SPACE-TIME METHOD

A. General formulation

In the GWST method [56–59], the Green's function (G), polarizability (P), dielectric function (ε), dynamically screened Coulomb interaction (W), and self-energy (Σ) are defined and stored in the real space (parameterized by the radius-vector $\mathbf{r}$) and imaginary time (τ) at a given temperature T, typically on appropriately constructed grids. The first approximation $G_0(\boldsymbol{r}\boldsymbol{r}'\tau)$ to the full interacting Green's function is constructed from the effective Hamiltonian where the electron-electron interactions are described by the exchange-correlation potential of the DFT [53] with the help of a standard approximation, such as, e.g., the LDA.

We define

$$G_0(\boldsymbol{r}\boldsymbol{r}'\tau) = \sum_k G_k^0(\tau)\psi_k(\boldsymbol{r})\psi_k^*(\boldsymbol{r}'), \tag{1}$$

with $G_k^0(\tau)$ the Green's function in the Kohn-Sham (KS) basis, which has the diagonal form

$$G_k^0(\tau) = -\theta(\xi_k)[1 - f_\beta(\xi_k)]e^{-\xi_k\tau} - \theta(-\xi_k)f_\beta(\xi_k)e^{\xi_k(\beta-\tau)}, \tag{2}$$

where k stands for the combined band- (l) quasimomentum ($\mathbf{k}$) index $k = \{l, \boldsymbol{k}\}$, f is the Fermi distribution function, and ξ_k and $\psi_k(\boldsymbol{r})$ are the KS Hamiltonian eigenvalues and eigenfunctions, respectively.

The irreducible polarizability is then found within the random phase approximation

$$P(\boldsymbol{r}\boldsymbol{r}'\tau) = G_0(\boldsymbol{r}\boldsymbol{r}'\tau)G_0^*(\boldsymbol{r}\boldsymbol{r}', -\tau), \tag{3}$$

and Fourier-transformed to the reciprocal space $P(\boldsymbol{r}\boldsymbol{r}'\tau) \to P(\boldsymbol{q}\boldsymbol{G}\boldsymbol{G}'\tau)$, where $\boldsymbol{q}$ and $\boldsymbol{G}$, $\boldsymbol{G}'$ are the quasimomentum in the Brillouin zone and reciprocal lattice vectors, correspondingly. To determine the screened interaction W from the polarizability via the Dyson equation algebraically, the function $P(\boldsymbol{q}\boldsymbol{G}\boldsymbol{G}'\tau)$ needs to be converted to the domain of the Matsubara frequency $i\omega$ by a Fourier transform (FT) $P(\boldsymbol{q}\boldsymbol{G}\boldsymbol{G}'\tau) \to P(\boldsymbol{q}\boldsymbol{G}\boldsymbol{G}'i\omega)$. The FT implementation depends on how the dependence of the imaginary time is represented: when a variable-step grid is used [46], the FT typically requires an interpolation onto one more suitable for the FT grid; in the Chebyshev-polynomial representation [60,61]; this extra operation is not needed for the FT. The specific details are discussed in the following section.

The inverse dielectric function, which accounts for dynamical screening of the Coulomb interaction, straightforwardly follows from $P(\boldsymbol{q}\boldsymbol{G}\boldsymbol{G}'i\omega)$ with the symmetrized version given as

$$\varepsilon^{-1}(\boldsymbol{q}\boldsymbol{G}\boldsymbol{G}', i\omega) = \left[\delta_{\boldsymbol{G}\boldsymbol{G}'} + 4\pi\frac{P(\boldsymbol{q}\boldsymbol{G}\boldsymbol{G}', i\omega)}{|\boldsymbol{q}+\boldsymbol{G}||\boldsymbol{q}+\boldsymbol{G}'|}\right]^{-1}, \tag{4}$$

and after the inverse FT $\varepsilon^{-1}(\boldsymbol{q}\boldsymbol{G}\boldsymbol{G}', i\omega) \to \varepsilon^{-1}(\boldsymbol{q}\boldsymbol{G}\boldsymbol{G}', \tau)$ yields

$$W(\boldsymbol{q}\boldsymbol{G}\boldsymbol{G}'\tau) = \sum_{\boldsymbol{q}\boldsymbol{G}\boldsymbol{G}'}\frac{4\pi}{\Omega}\frac{\varepsilon^{-1}(\boldsymbol{q}\boldsymbol{G}\boldsymbol{G}', \tau)}{|\boldsymbol{q}+\boldsymbol{G}||\boldsymbol{q}+\boldsymbol{G}'|}, \tag{5}$$

where Ω is the volume of the unit cell. Finally, the screened interaction is transformed to the direct space $W(\boldsymbol{q}\boldsymbol{G}\boldsymbol{G}'\tau) \to W(\boldsymbol{r}\boldsymbol{r}'\tau)$, so that the self-energy operator, $\Sigma(\boldsymbol{r}\boldsymbol{r}'\tau) = -G(\boldsymbol{r}\boldsymbol{r}'\tau)W(\boldsymbol{r}\boldsymbol{r}'\tau)$ and its matrix elements $\Sigma_{lm\mathbf{k}}(\tau) = \langle\psi_{l\mathbf{k}}|\Sigma(\boldsymbol{r}\boldsymbol{r}'\tau)|\psi_{m\mathbf{k}}\rangle$ could be computed. For further analysis, the self-energy matrix, denoted by $\hat{\Sigma}_\mathbf{k} \equiv \{\Sigma_{lm\mathbf{k}}\}$, is converted to the Matsubara frequency space by yet another FT, $\hat{\Sigma}_\mathbf{k}(\tau) \to \hat{\Sigma}_\mathbf{k}(i\omega)$.

We use two methods to extract the quasiparticle excitation energies. The first, traditional one, relies on analytic continuation of the self-energy to real frequencies. It is an intrinsically approximate approach, the accuracy of which is generally difficult to control since analytic continuation is fundamentally an ill-defined problem. However, numerically stable and physically meaningful results were obtained by first neglecting the off-diagonal matrix elements, which is typically justified for semiconductors, and finding the diagonal at real frequencies $\Sigma_{ll\mathbf{k}}(\omega)$ via fitting the $\Sigma_{ll\mathbf{k}}(i\omega)$ to a multipole expansion model [56–58]. This constitutes the simplest analytic continuation model. More generally, the Padé approximant technique suffers from the problems of numerical stability. It is worth mentioning other analytic continuation methods, more stable than the plain Padé, such as the averaged Padé approximant technique [70] and the Thieles reciprocal difference method applied in Ref. [71]. The quasiparticle (QP) energies are then found as solutions of the equation

$$\xi_{l\mathbf{k}}^{qp} = \xi_{l\mathbf{k}} + \mathrm{Re}\left[\Sigma_{ll\mathbf{k}}\left(\omega = \xi_{l\mathbf{k}}^{qp}\right)\right] - v_{l\mathbf{k}}^{\mathrm{xc}}, \tag{6}$$

where $v_{l\mathbf{k}}^{\mathrm{xc}}$ stands for the exchange-correlation potential used in the effective Hamiltonian to construct G_0, which needs to be subtracted to avoid double counting.

This approach is useful for providing an estimate of the QP spectrum, but, for the problem of determining the band gap, the additional approximation introduced by the analytic continuation is not necessary. The energy of excitations nearest to the Fermi level can be found in a controlled way from the asymptotic decay of the full Green's function at long imaginary times

$$|G_\mathbf{k}(\tau)| \to a_\mathbf{k}^e e^{-\xi_\mathbf{k}^e\tau} + a_\mathbf{k}^h e^{-|\xi_\mathbf{k}^h|(\beta-\tau)}, \tag{7}$$

$$\tau \gg [\xi^e]^{-1}, \quad [\beta-\tau] \gg |\xi^h|^{-1}, \tag{8}$$

where $a_\mathbf{k}^{e(h)}$ are some constants and $\xi^{e(h)}$ are the energies of the electron(hole)-like excitations. Here $G_\mathbf{k}$ can be taken as a sum over the band indices of the full Green's function matrix

$$G_\mathbf{k}(\tau) = \sum_{lm} G_{lm\mathbf{k}}(\tau), \tag{9}$$

where $G_{lm\mathbf{k}}(\tau)$ is obtained by solving the Dyson equation

$$\hat{G}_\mathbf{k}(i\omega) = \left[i\omega\hat{1} - \left(\hat{\Sigma}_\mathbf{k}(i\omega) - \hat{v}_\mathbf{k}^{xc}\right)\right]^{-1}, \tag{10}$$

with the subsequent FT $\hat{G}_\mathbf{k}(i\omega) \to \hat{G}_\mathbf{k}(\tau)$, where the matrix notation $\hat{G}_\mathbf{k} \equiv \{G_{lm\mathbf{k}}\}$ is used and $\hat{1}$ is the unity matrix. Following Eq. (7), the valence- (ξ^h) and conductance- (ξ^e) band energies can be extracted as linear fits of $\log[|G(\tau)|]$, as exemplified in Fig. 1 (discussed in more detail below).

Although the proposed scheme allows extracting the lowest excitation energies, other energies can, in principle, be computed, first, by fitting the untraced $G_{lm\mathbf{k}}(\tau)$ at diagonal. This corresponds to the assumption that the KS orbitals are a good approximation to the true quasiparticle ones. In those cases, where such approximation breaks down, one would have to apply a transformation of the Green's function to the basis of the quasiparticle orbitals estimated, for example, via the full quasiparticle equation with an analytically continued self-energy. It is not clear, however, if such a scheme should give an improvement over the pure analytic continuation one, but it is worth future studying.

The results obtained from Eq. (6) with the analytic continuation of the self-energy and those found from the asymptotic form of the Green's function (7) will be referred to as $G_0W_0^{AC}$ and $G_0W_0^{GF}$, respectively. We compare the energy band gaps extracted by both methods in the benchmark study of Si, Ge, and H in Sec. III B.

B. Details of implementation

The building-block functions (G, P, W, and Σ) in the *GW*ST technique decay fast with increasing the distance

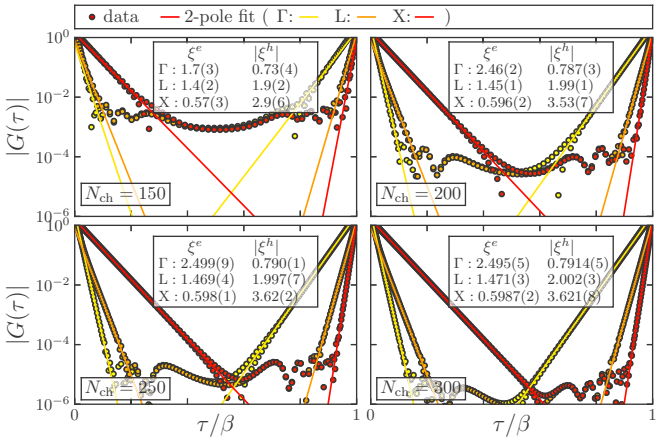

FIG. 1. The dependence of $G_{\mathbf{k}}$ on the imaginary time τ at high-symmetry k-points and the fit of its asymptotic behavior, Eq. (7), used to extract the valence- (ξ^h) and conductance- (ξ^e) band energies for Si shown as unframed numbers (in eV) with error bars in brackets. Note that left (right) columns of quasiparticle energies correspond to left (right) slopes of $G_{\mathbf{k}}(\tau)$ curves. Different panels correspond to different numbers of Chebyshev polynomials (framed numbers) used to represent $\hat{G}_{\mathbf{k}}(\tau)$. Color of a fitted line identifies a k-point in the way shown in the upper panel. Temperature was set to 300 K.

between $\mathbf{r}$ and $\mathbf{r}'$. Except for $\mathrm{W}(\mathbf{r},\mathbf{r}')$, which is long-ranged with $\sim 1/|\mathbf{r}-\mathbf{r}'|$ behavior. When storing functions of $\mathbf{r}$ and $\mathbf{r}'$, following the original nomenclature [56,58], we define the domain of the first argument $\mathbf{r}$ to be the unit cell (UC), which is put on a mesh of N_r points. The second argument $\mathbf{r}'$ is defined within the so-called interaction cell (IC). It is a larger domain with periodic boundary conditions, consisting of N_k unit cells. The size of the interaction cell defines the corresponding quasimomentum mesh in the Brillouin zone of N_k points. The specific crystal symmetries are used to reduce the memory consumption by storing all quantities on the irreducible wedge of the $\mathbf{r}$ coordinate grid, while the $\mathbf{r}'$ coordinate grid always has $N_r \times N_k$ size, spanning the IC.

Chebyshev polynomial (CP) representation provides an easily controllable way of storing and manipulating correlation functions in both time and frequency domains, as well as the Fourier transform algebra for switching between them. The concept is essentially that of representing a continuous function $F(\tau)$ as an expansion in an orthonormalized basis of polynomials $\{T_l(\tau)\}$, with the error controlled by the number of basis functions N_{ch} used in the representation

$$F(\tau) = \sum_{l=0}^{N_{ch}-1} F_l T_l(\tau), \tag{11}$$

$$F(i\omega) = \sum_{l=0}^{N_{ch}-1} F_l T_l(i\omega), \tag{12}$$

$$T_l(i\omega) = \int_0^\beta d\tau T_l(\tau) e^{i\omega\tau}. \tag{13}$$

Once the coefficients F_l are obtained, computing the Fourier transform is trivial with the help of the pretabulated functions $T_l(\tau)$ and $T_l(i\omega)$.

This framework was discussed in detail in Refs. [60,61] and applied to diverse systems in Ref. [61]. The methodology combines accuracy and simplicity and, therefore, can be straightforwardly used for the total energy calculation [61]. One should note that similar ideas are behind the *GW* implementation in the series of works [51,52,72–74], where the Chebyshev polynomials are used as well, however, with more sophisticated work flow with more control parameters. Another advanced scheme is known, the compressive sensing approach discussed in Ref. [75], which allows compressing the representation of the correlation functions greatly, and is worth future implementation.

It was shown in the original works [60,61] that for the basis $\{T_l(\tau), l = 0,\ldots,N_{ch}-1\}$ the optimal time mesh for sampling $F(\tau)$ in the calculation of F_l, must include exactly N_{ch} points:

$$\bar{\tau}_n = \tau\left[\cos\left(\pi\frac{2n+1}{2N_{ch}}\right)\right], \quad n = 0,\ldots,N_{ch}-1, \tag{14}$$

which are the roots of the higher-order polynomial $T_{N_{ch}}(\tau)$. Here the $\tau[x]$ function is a linear map from $[-1:1]$ to $[0:\beta]$: $\tau[x] = \beta(x+1)/2$, $-1 \leqslant x \leqslant 1$. Similarly, the points $i\bar{\omega}_n$, $n = 0,\ldots,N_{ch}-1$, for sampling the imaginary frequency dependence $F(i\omega)$ are chosen as roots of the Fourier transform counterpart $T_{N_{ch}}(i\omega)$, with a minor difference between the bosonic and fermionic cases [61]. The polynomial coefficients F_l are then obtained, either from the given imaginary-time $[F(\tau)]$ or frequency $[F(i\omega)]$ dependence, according to

$$\begin{aligned} F_l &= \sum_{n=0}^{N_{ch}-1} [A^{-1}]_{ln} F(\bar{\tau}_n) \\ &= \sum_{n=0}^{N_{ch}-1} [\widetilde{A}^{-1}]_{ln} F(i\bar{\omega}_n), \end{aligned} \tag{15}$$

with the transformation matrices A and $\widetilde{A}$ of size $N_{ch} \times N_{ch}$ defined by

$$\begin{aligned} A_{ln} &= T_l(\bar{\tau}_n), \\ \widetilde{A}_{ln} &= T_l(i\bar{\omega}_n). \end{aligned} \tag{16}$$

The coefficients F_l are sufficient to obtain both $F(\tau)$ or $F(i\omega)$ at any given argument through Eqs. (11) and (12).

The obvious disadvantage of this framework is that resolving the time dependence due to the states far away from the Fermi level requires a larger number of polynomials and corresponding grid points $\{\bar{\tau}_n\}$. This means that capturing the effects of core states or extremely high-energy empty states on the imaginary time dependence could be memory demanding. Having 100 bands for Si, we have to use 250 polynomials to achieve negligible discretization errors. However, the advantage of the CP framework is that, once the result is converged with N_{ch}, the systematic error of the FT is automatically negligible. Second, all-time/frequency-dependent functions are well represented in all regions of the time/frequency axis uniformly, which is essential for obtaining energies from the asymptotic behavior, Eq. (7). In addition, the Fourier transform $G(i\omega) \to G(\tau)$ generally requires a careful treatment of the high-frequency tail due to the slow convergence of

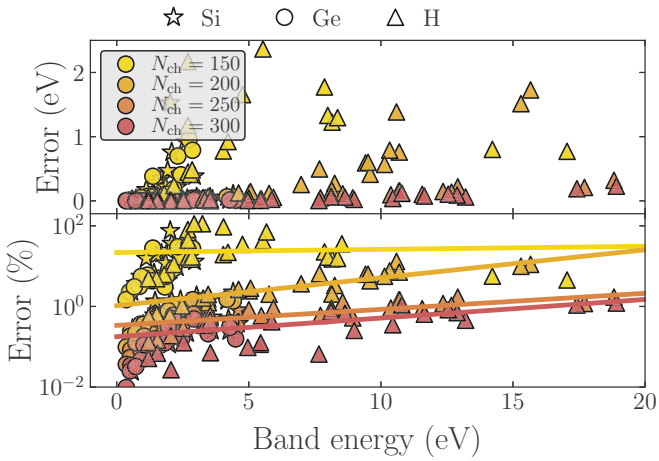

FIG. 2. Collection of (absolute) energy/error data points obtained by the fitting procedure depicted in Fig. 1 repeated for Si, Ge, and H across the BZ momentum points. Both absolute (top) and relative (bottom) errors are plotted as functions of band energy. Solid lines represent the fits to $f(x) = ae^{bx}$ functions of band energy x.

the truncation error. Still, the correct asymptotic is built in automatically in the CP representation.

Although the temperature was set to 300 K in all Matsubara time/frequency grids throughout this work, the presented framework can be used in a wide temperature range. The numerical cost for construction of Chebyshev polynomials in the imaginary-frequency domain grows with decreasing temperature due to a larger size of the nonsparsed Matsubara frequency grid for finding the roots of the N_{ch}th polynomial $T_{N_{ch}}(i\omega)$. This, however, is performed once before the GW calculations themselves, and therefore, the framework can be used even in a sub-Kelvin regime.

Finally, the scheme may find its applications, for example, in the diagrammatic Monte Carlo [62–68] calculations, where the correlation functions contain a numerical noise and AC-based approaches become unstable.

III. RESULTS: NEW SCHEMES

A. New estimation of QP energies

We demonstrate a procedure allowing for the extraction of the lowest QP energies from the imaginary-time GF asymptotic. We use Si and Ge as a validation set and compare the resulting band-gap values with available experimental data, but also consider the solid hydrogen under pressure (discussed in detail in Sec. IV) for the determination of the error bars. Figure 1 shows an example of the imaginary-time dependence of $G_{\mathbf{k}}$, Eq. (8), for Si computed with different values of N_{ch} and the result of the fit to the asymptotic form (7) used to determine the band gap in the $G_0W_0^{GF}$ approach. The fitting error behaves smoothly with the number of polynomials N_{ch} used in the CP representation. This can be seen when repeating the procedure shown in Fig. 1 for fitting the set of lowest QP energies for all studied materials over the Brillouin zone k-points. We see (Fig. 2) that the relative error has about two orders of magnitude variation with the band energy, not exceeding, however, 0.9% or 0.7% for Si and Ge, respectively, and 0.3%

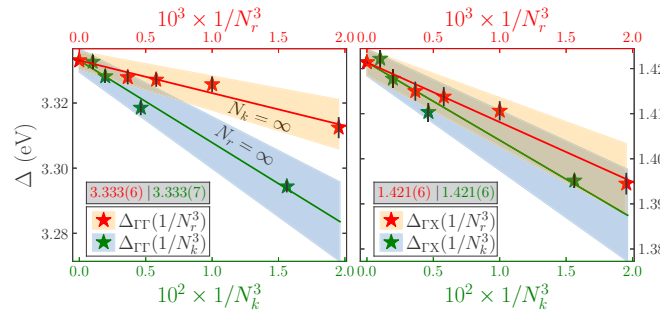

FIG. 3. Illustration of the algorithm behind the final extrapolation of $\Gamma \to \Gamma$ (left) and $\Gamma \to X$ (right) band gaps of Si to the infinite N_r and N_k grid parameters. Green/red data points correspond to $N_{r/k} = \infty$ columns/rows of the Table I ($G_0W_0^{GF}$ data) both carrying the data extrapolation error bars. The linear fit of these values to a $\sim\frac{1}{N_{k/r}}$ function is given by lines with associated fitting error bars shown by the shaded regions. The size of the shaded region is chosen to cover both the error of the fit itself and all error bars of data points.

for energy states within the relevant $[-3 : 3]$ eV window for 94 GPa pressurized hydrogen when taking $N_{ch} = 250$. It is evident that the error bar values reduce with decreasing the absolute of associated band energy values, and estimation at 94 GPa in the H case will give the upper error limit at higher pressures due to the reduction of the solid hydrogen's energy gap with pressure (e.g., see Sec. IV). Together with the extrapolation error discussed in the next section, these relative error estimations will be used when reporting the final QP energies and gaps. Consequently, all subsequent calculations will be done with $N_{ch} = 250$.

B. Extrapolation to infinite grid sizes

Table I shows that the AC and GF band gaps may differ by a ∼50 meV (Table I), which is due to both GF fitting and AC error bars (note that it is not possible to assess the AC error bar, as was discussed in Sec. II A). Figures 3–5 illustrate the convergence patterns of the $N_{k/r} = \infty$ rows/columns of Table I and the methodology behind the extrapolation to the infinity of both parameters for all studied compounds.

The estimation of the minimal gap of H is done by first interpolating the extracted QP energies from a regular k-point grid to the fine-sampled path connecting the high-symmetry reciprocal k-points and then by searching for the minimal gap

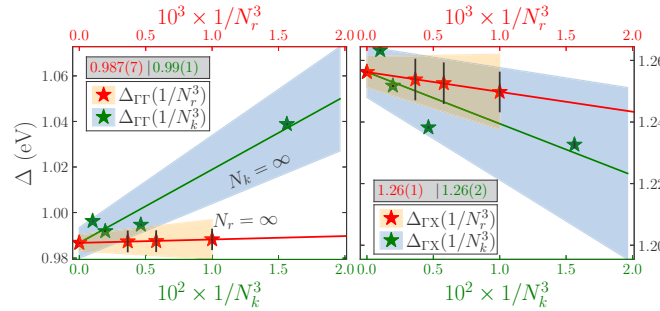

FIG. 4. Same as Fig. 3 but for Ge.

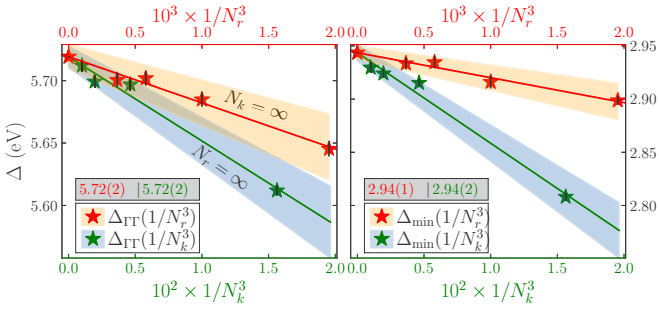

FIG. 5. Same as Fig. 3 but for H at 94 GPa with, however, a slightly different scheme for estimation of the $\Delta_{\min}$ (see Sec. III B).

value on the path. It is hard to assess the interpolation error bar explicitly. However, due to the fact that our extrapolation error bars are the same for direct (where no interpolation is needed) and minimal gaps for pressurised hydrogen, we can safely ignore this contribution.

Finally, our extrapolated gap values are compared with known results for Si and Ge in Table II.

IV. RESULTS: SOLID HYDROGEN

Recent x-ray diffraction experiment [37] of high-pressure hydrogen observed three Bragg peaks which are consistent with an $P6_3/mmc$ structure with c/a ratio close to $\sqrt{8/3}$ and the studied structure was reported as an isostructural hcp.

We considered a solid molecular structure with hexagonal closed pack hcp symmetry ($P6_3/mmc$) with four hydrogen atoms per primitive cell. Our DFT calculations were carried out using the QUANTUM ESPRESSO (QE) suite of programs [84] and the Becke-Lee-Yang-Parr (BLYP) [85] XC-DFT functional. We used a plane-waves basis set with an energy cutoff of 100 Ry. For the geometry and cell optimizations, a $16 \times 16 \times 16$ **k**-point mesh with the QE-tabulated standard norm-conserving pseudopotential is used. The quasi-Newton algorithm was used for all cell and geometry optimization, with a convergence threshold on the total energy and forces of 0.01 mRy and 0.1 mRy/Bohr, respectively. The DFT-BLYP band structure is calculated using a k-mesh of $24 \times 24 \times 24$.

Our band structure calculations (Fig. 6) show a conduction band minimum at the high-symmetry Γ-point. The valence band maximum occurs between K and Γ points. One can also observe a second valence band peak at the k-point between Γ and M points, which is (depending on the pressure) between 0.2 and 0.6 eV below the valence band maximum.

Increasing the pressure shifts the DFT and GW energy bands relative to the Fermi energy. The linear extrapolation to the zero band gaps was used for finding the metallization pressures (Fig. 7). The DFT static (without protons zero-point motion contribution) indirect and direct energy gaps vanish at 120(9) and 253(20) GPa, respectively. The $G_0W_0^{GF}$ indirect and direct static band gaps terminate at 149(10) and 270(18) GPa, respectively. The system's actual metallization pressure is P_{met}=149(10) GPa, where the indirect band gap vanishes and the lowest unoccupied energy state at the Γ point touch the Fermi energy. Hence, at $P > P_{\text{met}}$, the nature of the direct gap at the Γ point changes from the difference between the highest-occupied energy eigenstate (below the Fermi energy) and lowest-unoccupied state (above the Fermi energy) to the difference between the first two energy states below the Fermi energy at the Γ point. This difference becomes zero at 273(21) GPa. From the many-body point of view, the direct gap at the Γ point for $P < P_{\text{met}}$ represents the energy difference between adding an electron to the conduction band at the Γ point and removing an electron from the valence band

TABLE I. $\Gamma \to X$ energy band gap of Si and Ge (in eV) and minimal gap of pressurized hydrogen (more details in Sec. IV) obtained by $G_0W_0^{AC}$ and $G_0W_0^{GF}$ techniques at $T = 300$ K and at different quasimomentum and real space grids. The $N_{k/r} = \infty$ rows/columns are extrapolations of columns/rows of data to the infinite grids using the linear to $\frac{1}{N_{r/k}}$ fitting function. The final value for the gap, which is written into the cell of $N_{k/r} = \infty$ row/column crossing, is taken as an additional extrapolation of either $N_k = \infty$ row or $N_r = \infty$ column, the one with the largest error bar. The algorithm behind the final error bar estimation is visually illustrated in Figs. 3–5. Error bar of the time/frequency representation is not taken into account explicitly in this table.

k-mesh	$N_r = 8^3$	$N_r = 10^3$	$N_r = 12^3$	$N_r = 14^3$	$N_r = \infty$
		$\Gamma \to X$: Si-$G_0W_0^{AC}$			
$N_k = 4^3$	1.325	1.341	1.344	1.346	1.352(4)
$N_k = 6^3$	1.336	1.352	1.356	1.357	1.363(4)
$N_k = 8^3$	1.342	1.357	1.361	1.362	1.368(4)
$N_k = 10^3$	1.345	1.361	1.364	1.365	1.371(4)
$N_k = \infty$	1.344(3)	1.360(3)	1.363(2)	1.364(2)	1.371(6)
		$\Gamma \to X$: Si-$G_0W_0^{GF}$			
$N_k = 4^3$	1.372	1.385	1.389	1.390	1.395(3)
$N_k = 6^3$	1.384	1.400	1.403	1.404	1.410(4)
$N_k = 8^3$	1.391	1.407	1.410	1.411	1.418(4)
$N_k = 10^3$	1.396	1.412	1.415	1.416	1.422(4)
$N_k = \infty$	1.394(5)	1.411(4)	1.414(4)	1.415(4)	1.421(6)
		$\Gamma \to X$: Ge-$G_0W_0^{AC}$			
$N_k = 4^3$		1.192	1.195	1.196	1.200(1)
$N_k = 6^3$		1.218	1.222	1.223	1.2257(9)
$N_k = 8^3$		1.228	1.232	1.233	1.2359(9)
$N_k = 10^3$		1.235	1.238	1.239	1.2423(8)
$N_k = \infty$		1.235(5)	1.238(5)	1.239(5)	1.242(7)
		$\Gamma \to X$: Ge-$G_0W_0^{GF}$			
$N_k = 4^3$		1.223	1.228	1.229	1.233(2)
$N_k = 6^3$		1.231	1.235	1.236	1.2382(8)
$N_k = 8^3$		1.245	1.248	1.249	1.2518(4)
$N_k = 10^3$		1.256	1.260	1.261	1.2633(8)
$N_k = \infty$		1.25(1)	1.25(1)	1.25(1)	1.26(2)
		min. gap: H-$G_0W_0^{AC}$ (94 GPa)			
$N_k = 4^3$	2.751	2.765	2.781	2.789	2.79(1)
$N_k = 6^3$	2.849	2.868	2.885	2.884	2.895(7)
$N_k = 8^3$	2.851	2.868	2.886	2.884	2.894(8)
$N_k = 10^3$	2.842	2.853	2.872	2.871	2.88(1)
$N_k = \infty$	2.86(2)	2.88(3)	2.90(3)	2.89(3)	2.90(4)
		min. gap: H-$G_0W_0^{GF}$ (94 GPa)			
$N_k = 4^3$	2.770	2.785	2.801	2.799	2.808(7)
$N_k = 6^3$	2.868	2.889	2.905	2.904	2.915(7)
$N_k = 8^3$	2.878	2.897	2.915	2.913	2.924(8)
$N_k = 10^3$	2.890	2.903	2.922	2.921	2.93(1)
$N_k = \infty$	2.899(8)	2.92(1)	2.93(1)	2.93(1)	2.94(2)

TABLE II. A comparison between the $\Gamma \to \Gamma$ and $\Gamma \to X$ $G_0W_0^{GF}$ band gaps of Si and Ge together with a slice of theoretical G_0W_0 and experimental results. Energies are in eV. Error bars associated with band gaps are composed out of extrapolation to infinite grids and $G_0W_0^{GF}$ band energy extraction error bars.

Si		
Method	$\Gamma \to \Gamma$	$\Gamma \to X$
Space-time, GF (this work)	3.33(4)	1.42(2)
Space-time 1 (Ref. [58])	3.24	1.34
Space-time 2 (Ref. [58])	3.32	1.42
Plane-wave (Ref. [41])	3.35	1.44
Plane-wave (Ref. [76])	3.2	1.2
All-electron (Ref. [46])	3.12	
All-electron (Ref. [77])	3.30	
All-electron (Ref. [78])	3.15	
All-electron (Ref. [79])	3.16	1.11
Exp. (Ref. [80])	3.40	
Exp. (Ref. [81])	3.05	
Exp. (Ref. [41])	3.4	1.3
Exp. (Ref. [76])	3.37	1.25
Ge		
Method	$\Gamma \to \Gamma$	$\Gamma \to X$
Space-time, GF (this work)	0.99(2)	1.26(3)
Plane-wave (Ref. [82])		1.23
All-electron (Ref. [46])	1.11	0.49
All-electron (Ref. [79])	0.84	0.97
Exp. (Ref. [83])	1.0	1.3
Exp. (Ref. [82])	0.89	1.10

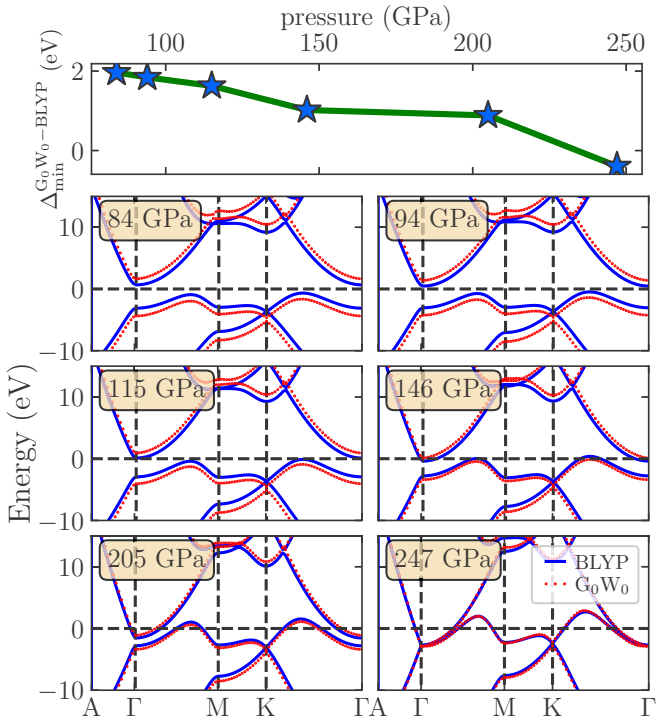

FIG. 6. (First panel from top) The $G_0W_0^{AC}$ band-gap enhancement over the DFT-BLYP for the hcp molecular solid hydrogen. (Other panels) The band structure of the hcp phase of hydrogen at different pressures calculated by DFT-BLYP and $G_0W_0^{AC}$. The valence band maximum is located ∼0.7 of the distance between Γ and K, and the conduction band minimum is at the Γ point.

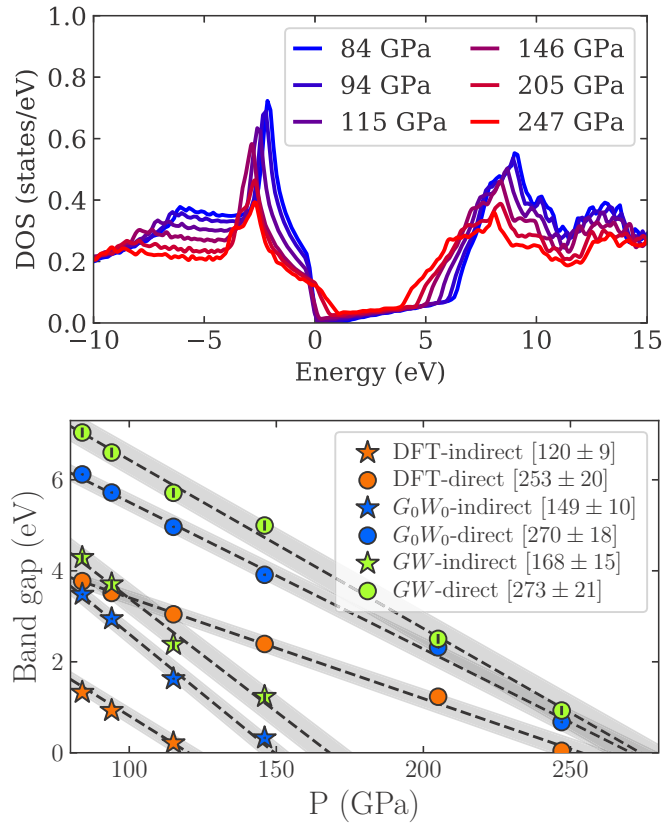

FIG. 7. (Top panel) The DFT-BLYP electronic density of states (DOS) of the hcp structure as a function of pressure. (Bottom panel) DFT-BLYP, G_0W_0 and fully self-consistent *GW* energy band gaps as a function of pressure. Dashed lines are the linear fit of the corresponding data points explained in the legend, where corresponding gap closure pressures are specified as well. Shadowed regions covering the data points and extrapolation error bars are used to determine the gap closure pressure error bars. Note the definition of the direct gap in the text.

at the same k-point. While the direct gap at the Γ point for $P_{\text{met}} < P < 273(21)$ is associated with the energy difference between removing an electron from the first and second states below the E_F at the Γ point.

The fixed-node diffusion quantum Monte Carlo (DMC) calculation suggested that in the majority of molecular structures of high-pressure solid hydrogen, the indirect energy band-gap reduction per pressure is ∼0.02 eV/GPa [34]. However, a linear fitting of G_0W_0 band gaps as a function of pressure yielded 0.05 and 0.03 eV/GPa indirect and direct band-gap reduction rates, respectively.

For the sake of comparison, we also performed the fully self-consistent *GW* (scGW) [86] calculations following the identical algorithms for QP energies extraction and the band gaps' extrapolation. The scGW indirect and direct band-gap closure points are at 170 and 273 GPa, respectively, and corresponding gap reduction rates are 0.05 and 0.037 eV/GPa. Since the self-consistent *GW* gaps are typically overestimated with respect to experiments, the resulting gap closure pressures should be seen as upper bounds.

The DFT-BLYP electronic density of states (DOS) (Fig. 7) illustrates that the indirect band-gap closure has a minor contribution to the DOS at the Fermi level. Instead, an essential

contribution originates from the hole-like bands crossing the Fermi level. Thus, it can be speculated that the system possibly behaves like a bad metal with properties similar to a semimetal at lower pressures, which has also been claimed by experiment [18].

So far, we discussed the static band-gap termination, meaning that the proton zero-point motion (ZPM) contribution, which reduces the energy band gap, is neglected. The effect of ZPM and ionic thermal contribution to the fundamental band-gap reduction, which is estimated using the path-integral-molecular-dynamic [87] and coupled electron-ion Monte Carlo [88], is 2–2.5 eV depending on the crystal structure of solid hydrogen and the pressure range. Recently the DFT-BLYP method was applied to a DFT-PBE predicted molecular structure, and the results predicted that nuclear quantum fluctuations can reduce the optical band gap by 3.0 eV and indirect gap by 2.0 eV [89]. Assuming the ZPM band-gap reduction is larger than 2 eV in both direct and indirect gaps, one can estimate that the $G_0W_0^{GF}$ + ZPM direct band gap terminates below ∼210 GPa, while the indirect one should close below ∼110 GPa.

Most of the experimental studies suggest that the metallic behavior of solid hydrogen arises only at pressures larger than ∼350 GPa. For instance, measurements by Eremets *et al*. predicted that at pressures of 350–360 GPa and $T < 200K$, the hydrogen starts to conduct with a semimetallic behavior [18]. Another report of a recent experiment [8] yields a discontinuous change of the direct band gap of high-pressure hydrogen, from 0.6 eV to below 0.1 eV at ∼425 GPa. The results were associated with forming a metallic state for the high-pressure hydrogen. Hence, the structure of high-pressure solid hydrogen has to have a finite energy band gap at pressures up to 350 GPa, which is not the case for the ordered hcp even without the ZPM contribution. We then conclude that the ordered hcp structure cannot be the right candidate for the structure of phase III of solid hydrogen due to the inconsistency between its $G_0W_0^{GF}$ metallization pressure and the experiment.

The local density approximation (LDA) single-particle energies were used in the GW quasiparticle calculations for determining the energy band gap of solid molecular hydrogen with orientationally ordered and disordered hcp structure [69]. It was predicted that the indirect band gap of the orientationally ordered structure becomes zero at 151 GPa, while the band-gap closure of the orientationally disordered phase takes place at 300 GPa. The spherical approximation, in which the potential of the nuclei is averaged isotropically over all possible molecular orientations [90], was used in determining the band gap of the orientationally disordered hcp phase. It was indicated that the metallization pressure of the orientationally disordered phase is almost two times larger than the ordered phase. In a more recent study [24], the path-integral-molecular-dynamic calculations predicted that the molecular orientational disorder and nuclear motions reduce the energy band gap and the metallization pressure of solid molecular hydrogen. One source of this discrepancy could be that the spherical approximation disregards the orientational coupling between molecules [91].

Our indirect quasiparticle band-gap closure of ordered structure agrees well with Ref.[69]. However, we believe that the effect of orientational distortion on the energy band gap requires further investigation, which is beyond the scope of our work.

V. CONCLUSION

We presented and discussed our implementation of the *GW* space-time method, which allows us to calculate the properties of extended systems at finite temperatures. We computed QP-energies using two approaches. In the first one, named $G_0W_0^{AC}$, the analytic continuation of the self-energy was employed. In our second approach $G_0W_0^{GF}$, we obtained the valence- and conductance-band energies from the asymptotic decay of the Green's function at long imaginary times. To validate our implementation, we calculated the energy band gap of two well-studied crystalline Si and Ge systems and compared our data with the experiment and established benchmark. We found that Chebyshev's representation of the imaginary time axis aws efficient at controlling the corresponding systematic errors in the numerical representation of G and W. Our robust results with controlled systematic errors within the *GW* approximation agree well with experiment and other published works.

With the same (maximal) cubic scaling with the system size as in other real-spaced based methods [51,71,73], the implementation of our scheme operates with the full quantities, and the storage requirement may be quite large, especially when dealing with larger systems and/or with more oscillating wave functions (e.g., transitional metals). In contrast, the scheme of Ref. [71] never required the full real-space object (G, W, or P) defined and, therefore, have better memory efficiency. Due to this reason, it can be used in combination with the PAW basis set for better precision. Moreover, the later work of Kutepov [92] showed a significant improvement to linear scaling in some stages of calculation, which is done by introducing the cutoff in the real space, which potentially can be implemented in the *GW* space-time method as well.

However, the *GW*ST scheme based on the norm-conserving pseudopotentials allows storing G and W fully in the allocatable memory for smaller systems, which allows for a quick stochastic sampling of the higher-order diagrams using the established DiagMC methodology [62–68]. DiagMC allows to stochastically sum the series in terms of G and W in a numerically exact way, with or without self-consistency, which can make calculations of materials properties fully controlled and reliable in the future.

Efficient sampling is relevant and representation for propagators is important, affecting the diagram's interpretation. For example, representing G and W in a basis set rather than as real-space quantities requires storing one of G or W as a four-dimensional (in basis index) array or including a nontrivial bare vertex element (e.g., which connects propagators represented in different bases) into the interpretation of the diagram. This brings additional complexity into the DiagMC both in calculations and in formalism. Therefore, having all quantities in the real space stored in the dynamic memory allocation eliminates these problems.

We applied our G_0W_0 technique to the problem of band-gap closure of solid hydrogen. We calculated the band structure and direct and indirect band gaps of orientationally ordered hcp molecular solid hydrogen. Considering the linear

behavior of the band gap with respect to pressure, the extrapolation of band gaps to zero indicates that the true metallization pressure of the hcp phase is ∼150 GPa. Considering zero-point motion (ZPM) electronic band renormalization, we estimated that G_0W_0 band gap would be closed at pressures below 110 GPa. One should note that there might be forces that directly increase the band gap and band-gap closure pressure or decrease the ZPM correction with pressure. Assuming the last scenario and noting that ZPM always reduces the band gap, we can take the $G_0W_0^{GF}$ result with around 150 GPa indirect band-gap closure pressure as an upper-pressure limit for the insulating hcp phase. However, most experimental data indicate that the solid hydrogen energy band gap at $T < 250$ K remains open up to ∼350 GPa. Thus, the structure of solid hydrogen at pressures below 350 GPa has to have a nonzero energy band gap. The comparison of our results with this experimental data rules out the possibility of realising a hcp structure in phase III of high-pressure solid hydrogen.

The fundamental energy band gap is indirect in most of the DFT-predicted molecular structures for phase III. By increasing the pressure, an indirect band-gap closure takes place before the direct band gap, and the metallization or semimetallization occurs through indirect band-gap termination. Correspondingly, some of the other PBE-DFT predicted candidates for phase III with indirect band gap at pressures above 300 GPa have symmetries of $C2/c$, $Cmca$, Pc, and $Pbcn$ with 24 (or 12), 24 (or 12), 48, and 48 number of hydrogen atoms per primitive unit cell. These structures are more complicated than hcp and deserve further investigation. Our approach allows us to study them systematically.

ACKNOWLEDGMENTS

This work was supported by the Simons Foundation as part of the Simons Collaboration on the Many-Electron Problem.

[1] E. Wigner and J. C. H. B. Huntington, J. Chem. Phys. **3**, 764 (1935).
[2] N. W. Ashcroft, Phys. Rev. Lett. **21**, 1748 (1968).
[3] E. Babaev, A. Sudbo, and N. W. Ashcroft, Nature (London) **431**, 666 (2004).
[4] S. A. Bonev, E. Schwegler, T. Ogitsu, and G. Galli, Nature (London) **431**, 669 (2004).
[5] H. K. Mao and R. J. Hemley, Rev. Mod. Phys. **66**, 671 (1994).
[6] V. L. Ginzburg, Phys. Usp. **42**, 353 (1999).
[7] J. M. McMahon, M. A. Morales, C. Pierleoni, and D. M. Ceperley, Rev. Mod. Phys. **84**, 1607 (2012).
[8] P. Loubeyre, F. Occelli, and P. Dumas, Nature (London) **577**, 631 (2020).
[9] R. M. Hazen, H. K. Mao, L. W. Finger, and R. J. Hemley, Phys. Rev. B **36**, 3944 (1987).
[10] M. I. Eremets and I. A. Troyan, Nat. Mater. **10**, 927 (2011).
[11] R. T. Howie, C. L. Guillaume, T. Scheler, A. F. Goncharov, and E. Gregoryanz, Phys. Rev. Lett. **108**, 125501 (2012).
[12] R. T. Howie, I. B. Magdău, A. F. Goncharov, G. J. Ackland, and E. Gregoryanz, Phys. Rev. Lett. **113**, 175501 (2014).
[13] A. F. Goncharov, I. Chuvashova, C. Ji, and H.-K. Mao, Proc. Natl. Acad. Sci. USA **116**, 25512 (2019).
[14] R. T. Howie, P. Dalladay-Simpson, and E. Gregoryanz, Nat. Mater. **14**, 495 (2015).
[15] P. Dalladay-Simpson, R. T. Howie, and E. Gregoryanz, Nature (London) **529**, 63 (2016).
[16] R. P. Dias and I. F. Silvera, Science **355**, 715 (2017).
[17] X. Liu, P. Dalladay-Simpson, R. T. Howie, B. Li, and E. Gregoryanz, Science **357**, eaan2286 (2017).
[18] M. I. Eremets, A. P. Drozdov, P. P. Kong, and H. Wang, Nat. Phys. **15**, 1246 (2019).
[19] C. J. Pickard and R. J. Needs, Nat. Phys. **3**, 473 (2007).
[20] C. J. Pickard, M. Martinez-Canales, and R. J. Needs, Phys. Rev. B **85**, 214114 (2012).
[21] A. F. Goncharov, J. S. Tse, H. Wang, J. Yang, V. V. Struzhkin, R. T. Howie, and E. Gregoryanz, Phys. Rev. B **87**, 024101 (2013).
[22] I. B. Magdău and G. J. Ackland, Phys. Rev. B **87**, 174110 (2013).
[23] I. I. Naumov, R. E. Cohen, and R. J. Hemley, Phys. Rev. B **88**, 045125 (2013).
[24] M. A. Morales, J. M. McMahon, C. Pierleoni, and D. M. Ceperley, Phys. Rev. B **87**, 184107 (2013).
[25] R. C. Clay, J. Mcminis, J. M. McMahon, C. Pierleoni, D. M. Ceperley, and M. A. Morales, Phys. Rev. B **89**, 184106 (2014).
[26] R. C. Clay, M. Holzmann, D. M. Ceperley, and M. A. Morales, Phys. Rev. B **93**, 035121 (2016).
[27] S. Azadi and T. D. Kühne, JETP Lett. **95**, 449 (2012).
[28] S. Azadi and W. M. C. Foulkes, Phys. Rev. B **88**, 014115 (2013).
[29] S. Azadi and G. J. Ackland, Phys. Chem. Chem. Phys., **19**, 21829 (2017).
[30] B. Monserrat, N. D. Drummond, P. Dalladay-Simpson, R. T. Howie, P. Lopez Ríos, E. Gregoryanz, C. J. Pickard, and R. J. Needs, Phys. Rev. Lett. **120**, 255701 (2018).
[31] S. Azadi, W. M. C. Foulkes, and T. D. Kühne, New J. Phys. **15**, 113005 (2013).
[32] S. Azadi, B. Monserrat, W. M. C. Foulkes, and R. J. Needs, Phys. Rev. Lett. **112**, 165501 (2014).
[33] N. D. Drummond, B. Monserrat, J. H. Lloyd-Williams, P. L. Ríos, C. J. Pickard, and R. J. Needs, Nat. Commun. **6**, 7794 (2015).
[34] S. Azadi, N. D. Drummond, and W. M. C. Foulkes, Phys. Rev. B **95**, 035142 (2017).
[35] S. Azadi and T. D. Kühne, Phys. Rev. B **100**, 155103 (2019).
[36] G. J. Ackland and J. S. Loveday, Phys. Rev. B **101**, 094104 (2020).
[37] C. Ji, B. Li, W. Liu, J. S. Smith, A. Majumdar, W. Luo, R. Ahuja, J. Shu, J. Wang, S. Sinogeikin, Y. Meng, V. B. Prakapenka, E. Greenberg, R. Xu, X. Huang, W. Yang, G. Shen, W. L. Mao, and H.-K. Mao, Nature (London) **573**, 558 (2019).
[38] S. Azadi and W. M. C. Foulkes, Phys. Rev. B **100**, 245142 (2019).
[39] Y. Yang, V. Gorelov, C. Pierleoni, D. M. Ceperley, and M. Holzmann, Phys. Rev. B **101**, 085115 (2020).

[40] G. Onida, L. Reining, and A. R. Rev, Rev. Mod. Phys. **74**, 601 (2002).
[41] M. S. Hybertsen and S. G. Louie, Phys. Rev. B **34**, 5390 (1986).
[42] F. Aryasetiawany and O. Gunnarsson, Rep. Prog. Phys. **61**, 237 (1998).
[43] M. P. Surh, S. G. Louie, and M. L. Cohen, Phys. Rev. B **43**, 9126 (1991).
[44] W. Luo, S. Ismail-Beigi, M. L. Cohen, and S. G. Louie, Phys. Rev. B **66**, 195215 (2002).
[45] B. Holm and U. von Barth, Phys. Rev. B **57**, 2108 (1998).
[46] W. Ku and A. G. Eguiluz, Phys. Rev. Lett. **89**, 126401 (2002).
[47] M. van Schilfgaarde, T. Kotani, and S. V. Faleev, Phys. Rev. Lett. **96**, 226402 (2006).
[48] T. Kotani, M. van Schilfgaarde, and S. V. Faleev, Phys. Rev. B **76**, 165106 (2007).
[49] S. V. Faleev, M. van Schilfgaarde, and T. Kotani, Phys. Rev. Lett. **93**, 126406 (2004).
[50] S. V. Faleev, M. van Schilfgaarde, T. Kotani, F. Léonard, and M. P. Desjarlais, Phys. Rev. B **74**, 033101 (2006).
[51] A. Kutepov, S. Y. Savrasov, and G. Kotliar, Phys. Rev. B **80**, 041103(R) (2009).
[52] A. L. Kutepov, Phys. Rev. B **95**, 195120 (2017).
[53] M. S. Hybertsen and S. G. Louie, Phys. Rev. Lett. **55**, 1418 (1985).
[54] J. McMinis, R. C. Clay, D. Lee, and M. A. Morales, Phys. Rev. Lett. **114**, 105305 (2015).
[55] G. E. Engel and B. Farid, Phys. Rev. B **47**, 15931 (1993).
[56] H. N. Rojas, R. W. Godby, and R. J. Needs, Phys. Rev. Lett. **74**, 1827 (1995).
[57] I. D. White, R. W. Godby, M. M. Rieger, and R. J. Needs, Phys. Rev. Lett. **80**, 4265 (1998).
[58] M. M. Rieger, L. Steinbeck, I. D. White, H. N. Rojas, and R. W. Godby, Comput. Phys. Commun. **117**, 211 (1999).
[59] L. Steinbeck, A. Rubio, I. White, R. Godby, L. Reining, and M. Torrent, Comput. Phys. Commun. **125**, 105 (2000).
[60] E. Gull, S. Iskakov, I. Krivenko, A. A. Rusakov, and D. Zgid, Phys. Rev. B **98**, 075127 (2018).
[61] J. Li, M. Wallerberger, N. Chikano, C.-N. Yeh, E. Gull, and H. Shinaoka, Phys. Rev. B **101**, 035144 (2020).
[62] N. V. Prokof'ev and B. V. Svistunov, Phys. Rev. Lett. **81**, 2514 (1998).
[63] E. Kozik, K. V. Houcke, E. Gull, L. Pollet, N. V. Prokof'ev, B. V. Svistunov, and M. Troyer, Europhys. Lett. **90**, 10004 (2010).
[64] K. V. Houcke, E. Kozik, N. V. Prokof'ev, and B. V. Svistunov, Phys. Procedia **6**, 95 (2010).
[65] A. S. Mishchenko, N. Nagaosa, and N. Prokof'ev, Phys. Rev. Lett. **113**, 166402 (2014).
[66] K. V. Houcke, F. Werner, E. Kozik, N. Prokof'ev, B. Svistunov, M. J. H. Ku, A. T. Sommer, L. W. Cheuk, A. Schirotzek, and M. W. Zwierlein, Nat. Phys. **8**, 366 (2012).
[67] Y. Deng, E. Kozik, N. V. Prokof'ev, and B. V. Svistunov, Europhys. Lett. **110**, 57001 (2015).
[68] K. Chen and K. Haule, Nat. Commun. **10**, 3725 (2019).
[69] H. Chacham and S. G. Louie, Phys. Rev. Lett. **66**, 64 (1991).
[70] J. Schött, I. L. M. Locht, E. Lundin, O. Grånäs, O. Eriksson, and I. Di Marco, Phys. Rev. B **93**, 075104 (2016).
[71] P. Liu, M. Kaltak, J. Klimeš, and G. Kresse, Phys. Rev. B **94**, 165109 (2016).
[72] Q. Yin, A. Kutepov, K. Haule, G. Kotliar, S. Y. Savrasov, and W. E. Pickett, Phys. Rev. B **84**, 195111 (2011).
[73] A. Kutepov, K. Haule, S. Y. Savrasov, and G. Kotliar, Phys. Rev. B **85**, 155129 (2012).
[74] A. L. Kutepov, Phys. Rev. B **94**, 155101 (2016).
[75] M. Kaltak and G. Kresse, Phys. Rev. B **101**, 205145 (2020).
[76] M. Grüning, A. Marini, and A. Rubio, J. Chem. Phys. **124**, 154108 (2006).
[77] N. Hamada, M. Hwang, and A. J. Freeman, Phys. Rev. B **41**, 3620 (1990).
[78] B. Arnaud and M. Alouani, Phys. Rev. B **62**, 4464 (2000).
[79] M. van Schilfgaarde, T. Kotani, and S. V. Faleev, Phys. Rev. B **74**, 245125 (2006).
[80] K.-H. Hellwege and O. Madelung, *Landolt-Börnstein, Numerical Data and Functional Relationships in Science and Technology*, Vol. 17a, New Series, Group III, (Springer, Berlin, 1982).
[81] J. E. Ortega and F. J. Himpsel, Phys. Rev. B **47**, 2130 (1993).
[82] E. L. Shirley, X. Zhu, and S. G. Louie, Phys. Rev. Lett. **69**, 2955 (1992).
[83] *Landolt-Börnstein, Zahlenwerte und Funktionen aus Naturwissenschaften und Technik*, Vol. III, New Series, K.-H. Hellwege and A. M. Hellwege (Eds.) (Springer-Verlag, New York, 1982).
[84] P. Giannozzi, S. Baroni, N. Bonini, M. Calandra, R. Car, C. Cavazzoni, D. Ceresoli, G. L. Chiarotti, M. Cococcioni, I. Dabo *et al.*, J. Phys.: Condens. Matter **21**, 395502 (2009).
[85] C. Lee, W. Yang, and R. G. Parr, Phys. Rev. B **37**, 785 (1988).
[86] P. García-González and R. W. Godby, Phys. Rev. B **63**, 075112 (2001).
[87] S. Azadi, R. Singh, and T. D. Kühne, J. Comput. Chem. **39**, 262 (2018).
[88] V. Gorelov, M. Holzmann, D. M. Ceperley, and C. Pierleoni, Phys. Rev. Lett. **124**, 116401 (2020).
[89] L. Monacelli, I. Errea, M. Calandra, and F. Mauri, Nat. Phys. **17**, 63 (2021).
[90] D. M. Wood and N. W. Ashcroft, Phys. Rev. B **25**, 2532 (1982).
[91] N. W. Ashcroft, Phys. Rev. B **41**, 10963 (1990).
[92] A. Kutepov, Comput. Phys. Commun. **257**, 107502 (2020).